nature biomedical engineering

SUPPLEMENTARY INFORMATION

https://doi.org/10.1038/s41551-018-0201-6

In the format provided by the authors and unedited.

Needle-shaped ultrathin piezoelectric microsystem for guided tissue targeting via mechanical sensing

Xinge Yu[1,2,19], Heling Wang[3,4,5,19], Xin Ning[2,19], Rujie Sun[2,6], Hassan Albadawi[7], Marcela Salomao[8], Alvin C. Silva[9], Yang Yu[2,10], Limei Tian[2,11], Ahyeon Koh[12], Chan Mi Lee[2], Aditya Chempakasseril[2], Peilin Tian[2], Matt Pharr[13], Jianghong Yuan[3,4,5,14], Yonggang Huang[3,4,5]*, Rahmi Oklu[7]* and John A. Rogers[1,2,5,15,16,17,18]*

[1]Simpson Querrey Center and Feinberg School of Medicine, Center for Bio-Integrated Electronics, Northwestern University, Evanston, IL, USA. [2]Department of Materials Science and Engineering, Frederick Seitz Materials Research Laboratory, University of Illinois at Urbana-Champaign, Urbana, IL, USA. [3]Department of Civil and Environmental Engineering, Northwestern University, Evanston, IL, USA. [4]Department of Mechanical Engineering, Northwestern University, Evanston, IL, USA. [5]Department of Materials Science and Engineering, Northwestern University, Evanston, IL, USA. [6]Advanced Composites Centre for Innovation and Science, University of Bristol, Bristol, UK. [7]Division of Vascular and Interventional Radiology, Minimally Invasive Therapeutics Laboratory, Mayo Clinic, Phoenix, AZ, USA. [8]Department of Pathology, Mayo Clinic, Phoenix, AZ, USA. [9]Division of Abdominal Imaging, Mayo Clinic, Phoenix, AZ, USA. [10]Department of Materials Science and Engineering, Tsinghua University, Beijing, China. [11]Beckman Institute for Advanced Science and Technology, University of Illinois at Urbana-Champaign, Urbana, IL, USA. [12]Department of Biomedical Engineering, Binghamton University, Binghamton, NY, USA. [13]Department of Mechanical Engineering, Texas A&M University, College Station, TX, USA. [14]Center for Mechanics and Materials, and Applied Mechanics Laboratory, Department of Engineering Mechanics, Tsinghua University, Beijing, China. [15]Department of Biomedical Engineering, Northwestern University, Evanston, IL, USA. [16]Department of Neurological Surgery, Northwestern University, Evanston, IL, USA. [17]Department of Chemistry, Northwestern University, Evanston, IL, USA. [18]Department of Electrical Engineering and Computer Science, Northwestern University, Evanston, IL, USA. [19]These authors contributed equally: Xinge Yu, Heling Wang and Xin Ning. *e-mail: y-huang@northwestern.edu; oklu.rahmi@mayo.edu; jrogers@northwestern.edu

© 2018 Macmillan Publishers Limited, part of Springer Nature. All rights reserved.

List of contents:

Supplementary Note 1. Finite element analysis (FEA) method and condition.

Supplementary Note 2. FEA validation of the scaling law.

Figure S1. Schematic illustration of procedures for fabricating PZT membrane inks on a SiO_2/Si wafer. a. Schematic diagram of cross section view for a PZT wafer with structure Au/Cr/PZT/Pt/Ti/SiO_2/Si. b. The capacitor structure PZT membranes were patterned and defined by photolithography technique. c. Partial under cut etching of SiO_2 sacrificial layer by buffered oxide etchant. d. Final PZT membrane inks formed by fully under cut etching of SiO_2 sacrificial layer with dilute HF solution.

Figure S2. Optical images of PZT membrane inks. a. PZT membrane inks array. b. Zoom in view of a PZT membrane.

Figure S3. Representation of transfer printing PZT membranes using a stamp with a post, showing individual process steps. a. Translation and Alignment to PZT membranes donor wafer. b. Selective engagement with one PZT membrane. c. a PZT membrane retrieval from donor wafer and contact to transfer onto polyimide (PI) acceptor substrate. d. e. Repeat cycles of steps a to c, zoom in view shows the two PZTs which will act as the sensor and actuator.

Figure S4. Schematic illustration of sensors/actuators encapsulation and electrodes formation process. a. a PZT membrane on polyimide (PI) substrate. b. First encapsulation PI layer spun and cured on top of the PZT membrane, then patterned using photo resist (PR). c. Opening to holes for cathode and anode connection by dry etching. d. Patterning PI for metallic interconnection wire deposition. e. Cr(10 nm)/Au(200 nm) interconnection wire deposition by E=-beam onto the PR and then remove additional PR by lift off technique. f. Final PI encapsulation layer deposited onto the devices to prevent influence of liquid during test.

Figure S5. Modulus probe design and images. a. Design of 6 modulus probes array for laser cut. b. Photograph of modulus probe devices done by laser cut. c. SEM image of a modulus probe device. d, e. Zoom in view of the modulus probe device, shown sensor area (c), and actuator area (d).

Figure S6. Photography of modulus sensor devices. a. Free standing polyimide (PI) supporting layer based device. b. Biopsy needle based device.

Figure S7. a. The nonlinear single-variable function *G* in the scaling law, determined by FEA. b. Simulation result of $V_{sensor}/V_{actuator}$ as a function of modulus.

Figure S8. Validation of the scaling law. a. validate that the function G depends only on a single combination of parameters, $(E_{\mathrm{Tissue}}d^3)/(E_{\mathrm{PI}}h_{\mathrm{PI}}^3)$. b. Validate the linear proportionality between the sensor voltage and $(A_{\mathrm{PZT}}h_{\mathrm{PZT}})/(E_{\mathrm{PI}}h_{\mathrm{PI}}d^2)$.

Figure S9. Prediction of the critical tissue modulus by the scaling law (black solid lines) and the FEA based on the geometrical dimensions of the device in the main text (red dots). a. Influence of the needle substrate modulus. b. Influence of the needle substrate thickness. c. Influence of spacing between the actuator and the sensor.

Figure S10. FEA prediction of the output voltage as a function of the tissue modulus for a small sample (size 1.0 mm × 1.0 mm × 1.5 mm)

Figure S11. Tension stress-strain plots of artificial agarose gel in quasi-static strain rate regimes, with different modulus values.

Figure S12. Experimental and theoretical analysis of the free standing device operation. Voltage output of sensor as a function of actuator voltage, measured on ten different agarose gels with known moduli, separately evaluated by quasi-static dynamical mechanical analysis shown in Figure S11. Here, the symbols and lines correspond to experimental (E) and theoretical (T) results, respectively. Error bars correspond to calculated standard error deviation.

Figure S13. The mechanism of deformation for the modulus sensors integrated on a biopsy needle. The red arrows indicate that the deformation induced by the actuator is transferred to the sensor mainly via the deformation of the tissue and also the PDMS below the PI substrate.

Figure S14. Theoretical analysis of biopsy needle based modulus sensor devices. a. Influence of the PDMS modulus on the sensor voltage. b. Influence of the PDMS thickness on the sensor voltage.

Figure S15. Theoretical analysis of V_{sensor} as a function of modulus, with actuator voltage of 5V.

Figure S16. Experimental analysis and modulus measurements of multilayer artificial tissues. a. Modulus measurement on a multilayer sample, with three different modulus of 18, 33, and 80 kPa. b. Sensor voltage and modulus values at an actuation voltage of 5V, as a function of inject depth of the multilayer sample.

Figure S17. Modulus measurements modulus as function of time for 60 minutes. a. Measured on artificial agarose gel tissues with different modulus values. b. Measured on big tissues, including liver, fat, kidney, and muscle.

Figure S18. Illustration of surgical procedures for modulus measurement on the rat.

Figure S19. Ex-vivo measurement of organ tissues of the rat. Device insert and measure on liver, a, lung b, spleen c, fat d, and kidney e.

Figure S20. Real-time modulus measurement by a biopsy needle device. The device traverse from cirrhosis liver to tumor. Error bars correspond to calculated standard error deviation.

Figure S21. Images of a cirrhotic liver with hepatocellular carcinoma. a. Measured by Magnetic resonance image (MRI). b. Measured by Magnetic resonance electrography (MRE), shown stiffness mapping of the whole cross section of the patient.

Figure S22. Image-guided modulus test. a,b, Photographs of a free standing device (device 1) injected into the non-tumor area of liver (a), and tumor (b). c,d, Photographs of a biopsy needle device (device 2) injected into the non-tumor area of liver (c), and tumor (d).

Supplementary Note 1: Finite element analysis (FEA) method and condition

FEA was conducted using the commercial software ABAQUS (version 6.14, Standard). The end of the needle outside the tissue was fixed to constrain the rigid body motion. Since the deformation was very small (strain <0.1 %), linear coupled mechanical-electric analysis was used to obtain the deformation and sensor voltage. The actuator and sensor were modelled by the linear piezoelectric material, and the tissue, PI and metals were modelled by the linear elastic material. The number of mesh in the model was ~10^6, with refinement around the region with the actuator and the sensor such that the minimum mesh size was 1/10 of the actuator/sensor size. The mesh convergence of the simulation was guaranteed for all cases.

3D solid elements are used to model the tissue and 3D shell elements are used to model the needle substrate, the actuator, the sensor and the electrode (Ti, Pt, Cr and Cu), with Figure S5 showing the layout. The needle is perfectly bonded to the tissue without relative slipping in FEA.

The material parameters are E_{PI}=2.5 GPa, ν_{PI}=0.34, E_{Ti}=110 GPa, ν_{Ti}=0.32, E_{Pt}=168 GPa, ν_{Pt}=0.38, E_{Cr}=279 GPa, ν_{Cr}=0.21, E_{Cr}=117 GPa, ν_{Cu}=0.36. The constitutive model for PZT is

$$\begin{Bmatrix}\sigma_{11}\\ \sigma_{22}\\ \sigma_{33}\\ \sigma_{23}\\ \sigma_{31}\\ \sigma_{12}\end{Bmatrix}=\begin{bmatrix}C_{11} & C_{12} & C_{13} & 0 & 0 & 0\\ C_{12} & C_{11} & C_{13} & 0 & 0 & 0\\ C_{13} & C_{13} & C_{33} & 0 & 0 & 0\\ 0 & 0 & 0 & C_{44} & 0 & 0\\ 0 & 0 & 0 & 0 & C_{44} & 0\\ 0 & 0 & 0 & 0 & 0 & C_{66}\end{bmatrix}\begin{Bmatrix}\varepsilon_{11}\\ \varepsilon_{22}\\ \varepsilon_{33}\\ 2\varepsilon_{23}\\ 2\varepsilon_{31}\\ 2\varepsilon_{12}\end{Bmatrix}-\begin{bmatrix}0 & 0 & e_{31}\\ 0 & 0 & e_{31}\\ 0 & 0 & e_{33}\\ 0 & e_{15} & 0\\ e_{15} & 0 & 0\\ 0 & 0 & 0\end{bmatrix}\begin{Bmatrix}E_1\\ E_2\\ E_3\end{Bmatrix} \quad \text{(S1)}$$

$$\begin{Bmatrix}D_1\\ D_2\\ D_3\end{Bmatrix}=\begin{bmatrix}0 & 0 & 0 & 0 & e_{15} & 0\\ 0 & 0 & 0 & e_{15} & 0 & 0\\ e_{31} & e_{31} & e_{33} & 0 & 0 & 0\end{bmatrix}\begin{Bmatrix}\varepsilon_{11}\\ \varepsilon_{22}\\ \varepsilon_{33}\\ 2\varepsilon_{23}\\ 2\varepsilon_{31}\\ 2\varepsilon_{12}\end{Bmatrix}+\begin{bmatrix}k_{11} & 0 & 0\\ 0 & k_{11} & 0\\ 0 & 0 & k_{33}\end{bmatrix}\begin{Bmatrix}E_1\\ E_2\\ E_3\end{Bmatrix} \quad \text{(S2)}$$

where σ_{ij} , ε_{ij} , E_i and D_i are the stress, strain, electrical filed and electrical displacement respectively. The elastic parameters are C_{11}=110 GPa, C_{12}=63 GPa, C_{13}=64 GPa, C_{33}=100 GPa, C_{44}=20 GPa and C_{66}=(C_{11} -C_{12})/2. The piezoelectric parameters are e_{31}=−9.6 N /(V·m), e_{33}=15.1 N /(V·m), and e_{15}=12.0 N /(V·m). The dielectric parameters are k_{33} =852ε_0, where ε_0 is the vacuum permittivity.

Supplementary Note 2: FEA validation of the scaling law

The scaling law Eq. (1) in the main text is validated by FEA for $h_{\mathrm{PZT}} \ll h_{\mathrm{PI}} \ll w_{\mathrm{PI}}, L_{\mathrm{PI}}$, and $h_{\mathrm{PZT}} \ll L_{\mathrm{PZT}}$, $w_{\mathrm{PZT}} \ll d \ll w_{\mathrm{PI}}, L_{\mathrm{PI}}$. First, the function G is validated to depend only on a single combination of parameters, $(E_{\mathrm{Tissue}} d^3)/(E_{\mathrm{PI}} h_{\mathrm{PI}}^3)$. Among four parameters E_{Tissue}, d, E_{PI} and h_{PI}, one changes while the other three are fixed. The sensor voltage obtained by FEA then gives G, which is shown by the G~$(E_{\mathrm{Tissue}} d^3)/(E_{\mathrm{PI}} h_{\mathrm{PI}}^3)$ plot in Figure S2a. It is clear that all data points fall on the same curve, confirming that G depends only on G~$(E_{\mathrm{Tissue}} d^3)/(E_{\mathrm{PI}} h_{\mathrm{PI}}^3)$.

The linear proportionality between the sensor voltage and $(A_{\mathrm{PZT}} h_{\mathrm{PZT}})/(E_{\mathrm{PI}} h_{\mathrm{PI}} d^2)$ is verified next. With G fixed, among five parameters d, E_{PI}, h_{PI}, A_{PZT} and h_{PZT}, one changes while the other four are fixed. All data points obtained by FEA fall on the straight line in Figure S2b, confirming that the sensor voltage is linearly proportional to $(A_{\mathrm{PZT}} h_{\mathrm{PZT}})/(E_{\mathrm{PI}} h_{\mathrm{PI}} d^2)$.

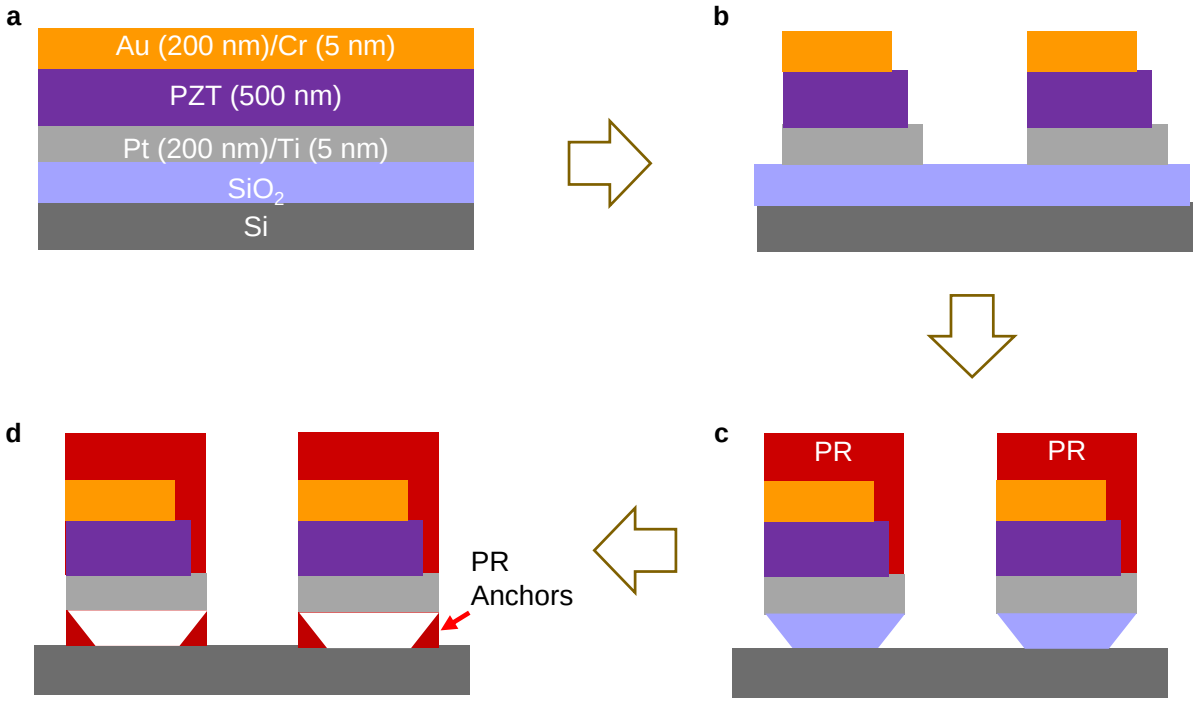

Figure S1. Schematic illustration of procedures for fabricating PZT membrane inks on a SiO_2/Si wafer. **a**. Schematic diagram of cross section view for a PZT wafer with structure Au/Cr/PZT/Pt/Ti/SiO_2/Si. **b**. The capacitor structure PZT membranes were patterned and defined by photolithography technique. **c**. Partial under cut etching of SiO_2 sacrificial layer by buffered oxide etchant. **d**. Final PZT membrane inks formed by fully under cut etching of SiO_2 sacrificial layer with dilute HF solution.

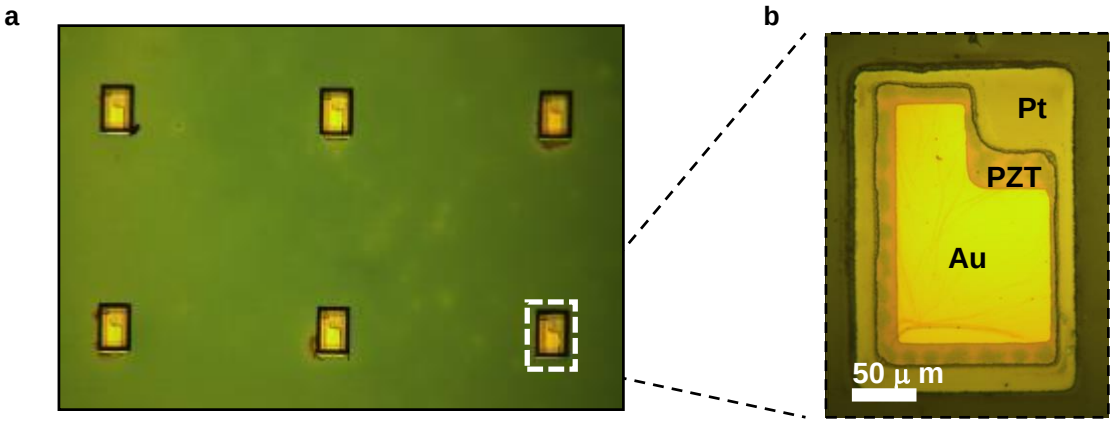

Figure S2. Optical images of PZT membrane inks. **a**. PZT membrane inks array. **b**. Zoom in view of a PZT membrane

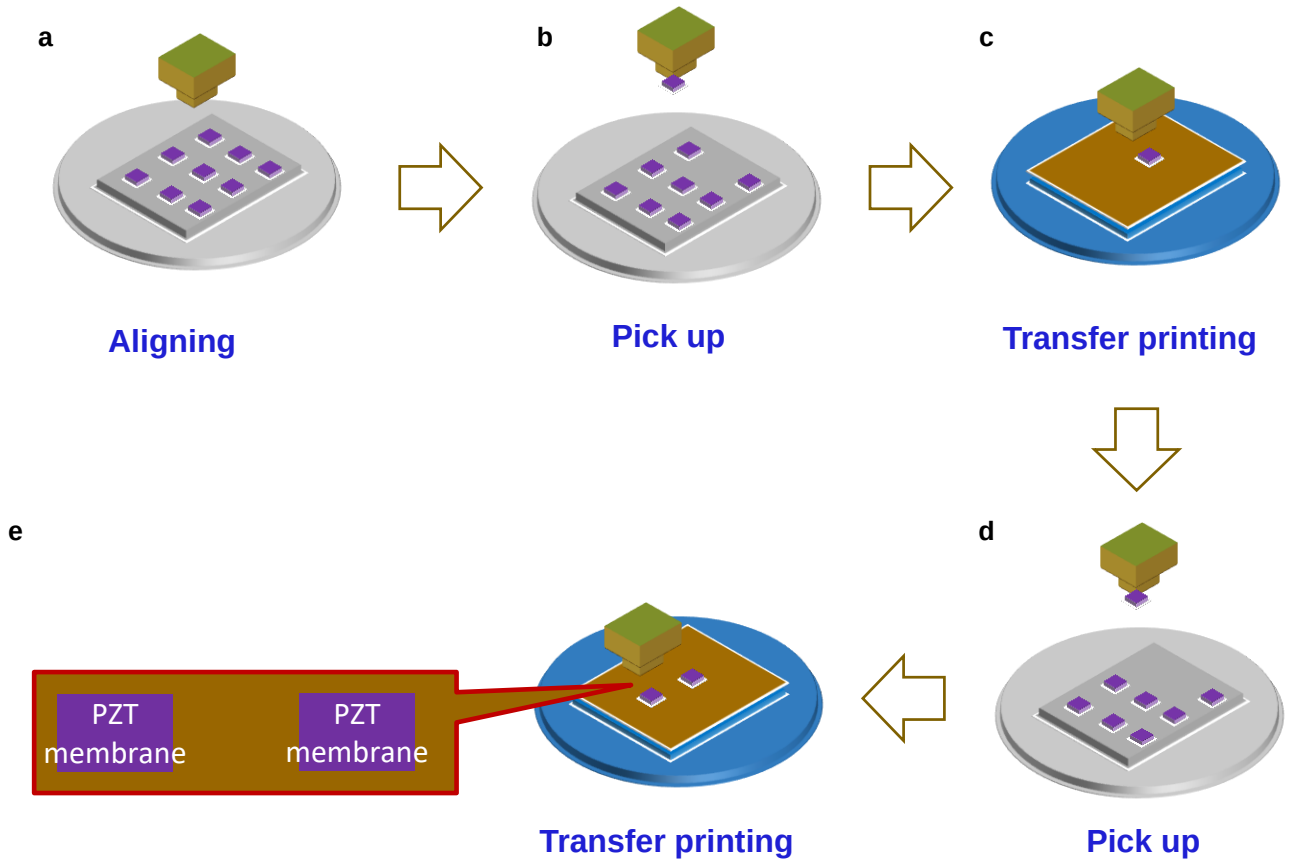

Figure S3. Representation of transfer printing PZT membranes using a stamp with a post, showing individual process steps. a. Translation and Alignment to PZT membranes donor wafer. **b**. Selective engagement with one PZT membrane. **c**. a PZT membrane retrieval from donor wafer and contact to transfer onto polyimide (PI) acceptor substrate. **d**. **e**. Repeat cycles of steps a to c, zoom in view shows the two PZTs which will act as the sensor and actuator.

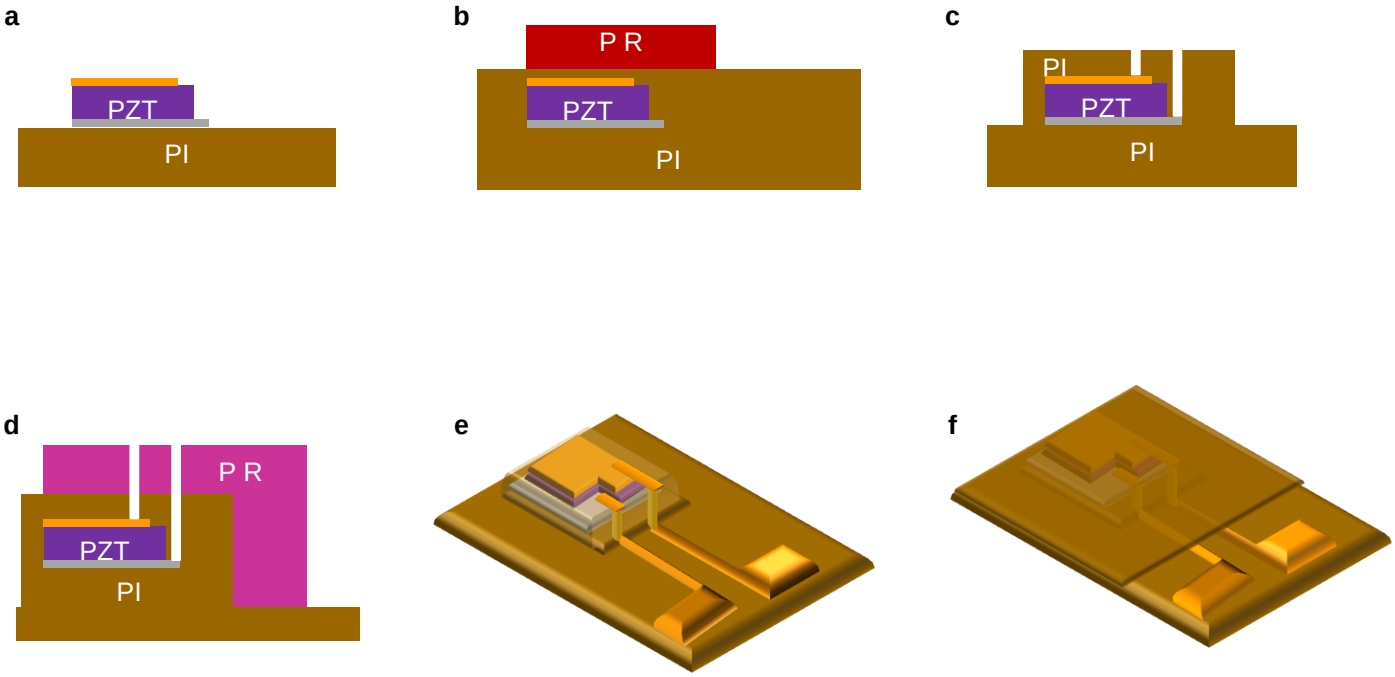

Figure S4. Schematic illustration of sensors/actuators encapsulation and electrodes formation process. a. a PZT membrane on polyimide (PI) substrate. **b**. First encapsulation PI layer spun and cured on top of the PZT membrane, then patterned using photo resist (PR). **c**. Opening to holes for cathode and anode connection by dry etching. **d**. Patterning PI for metallic interconnection wire deposition. **e**. Cr(10 nm)/Au(200 nm) interconnection wire deposition by E=-beam onto the PR and then remove additional PR by lift off technique. **f**. Final PI encapsulation layer deposited onto the devices to prevent influence of liquid during test.

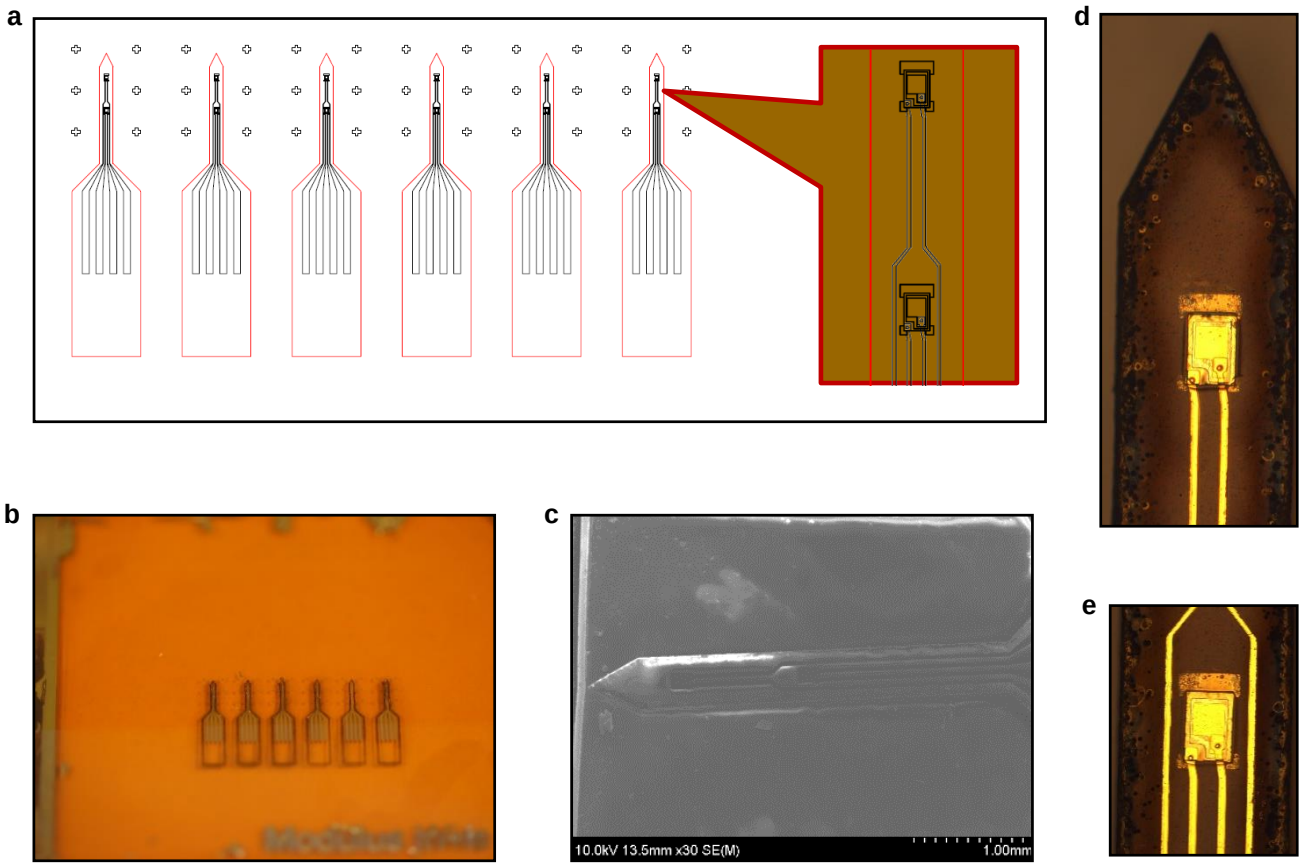

Figure S5. Modulus probe. a. Design of 6 modulus probes array for laser cut. **b**. Photograph of modulus probe devices done by laser cut. **c**. SEM image of a modulus probe device. **d, e.** Zoom in view of the modulus probe device, shown sensor area (c), and actuator area (d).

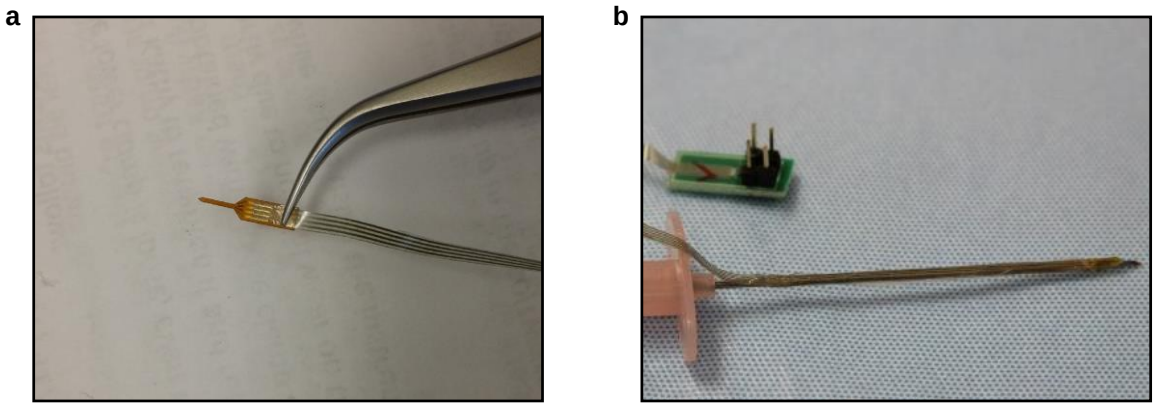

Figure S6. Photography of modulus sensor devices. a. Free standing polyimide (PI) supporting layer based device. **b**. Biopsy needle based device.

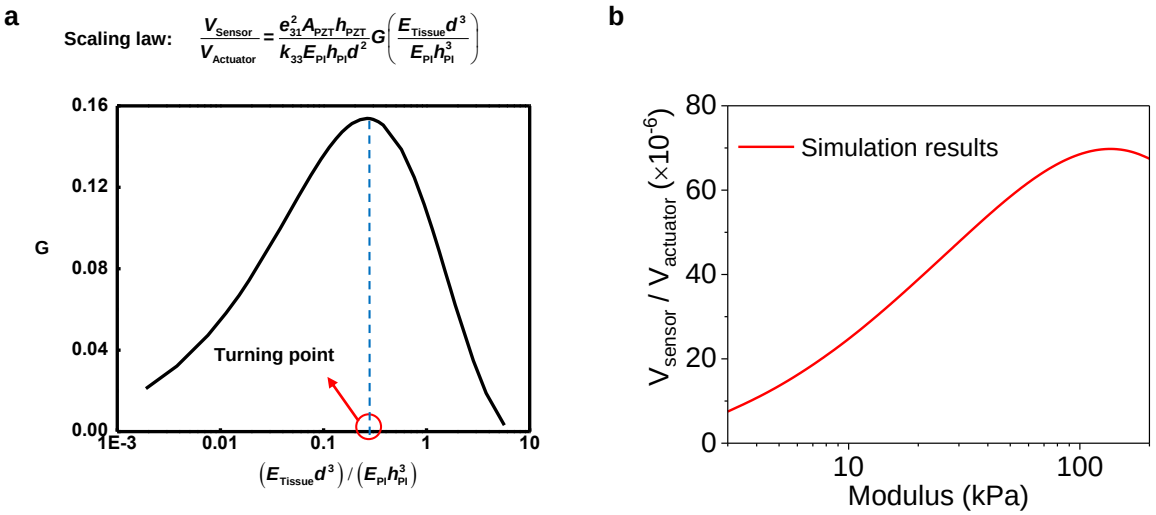

Figure S7. a. The nonlinear single-variable function *G* in the scaling law, determined by FEA. **b.** Simulation result of $V_{sensor}/V_{actuator}$ as a function of modulus

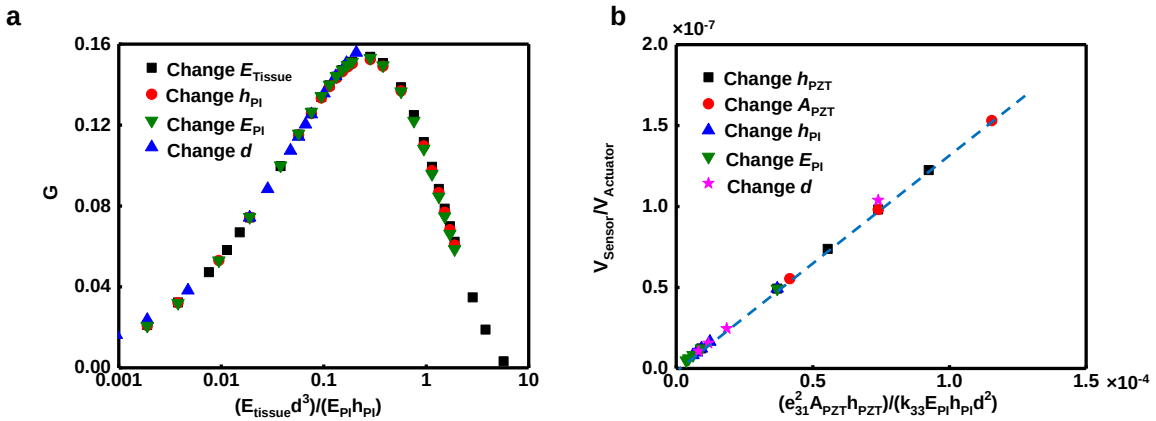

Figure S8. Validation of the scaling law. a. validate that the function G depends only on a single combination of parameters, $(E_{\mathrm{Tissue}}d^3)/(E_{\mathrm{PI}}h_{\mathrm{PI}}^3)$. **b.** Validate the linear proportionality between the sensor voltage and $(A_{\mathrm{PZT}}h_{\mathrm{PZT}})/(E_{\mathrm{PI}}h_{\mathrm{PI}}d^2)$.

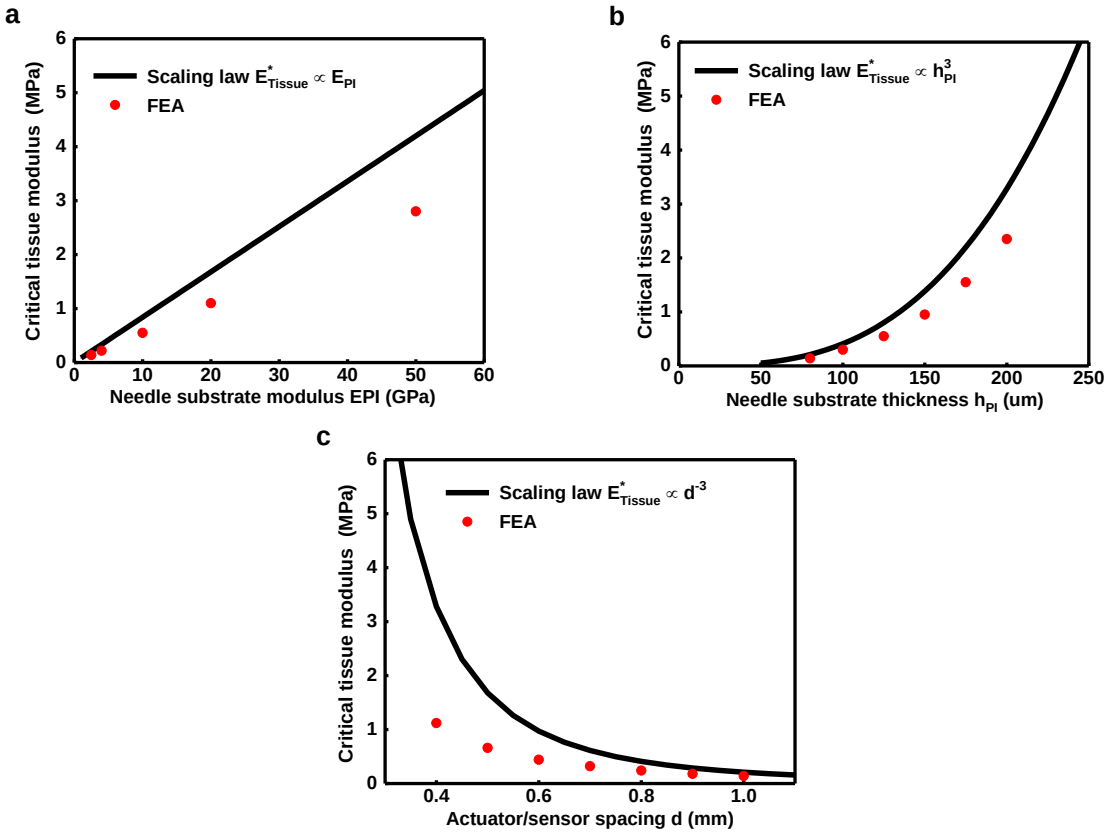

Figure S9. Prediction of the critical tissue modulus by the scaling law (black solid lines) and the FEA based on the geometrical dimensions of the device in the main text (red dots). **a.** influence of the needle substrate modulus. **b.** influence of the needle substrate thickness. **c.** influence of spacing between the actuator and the sensor.

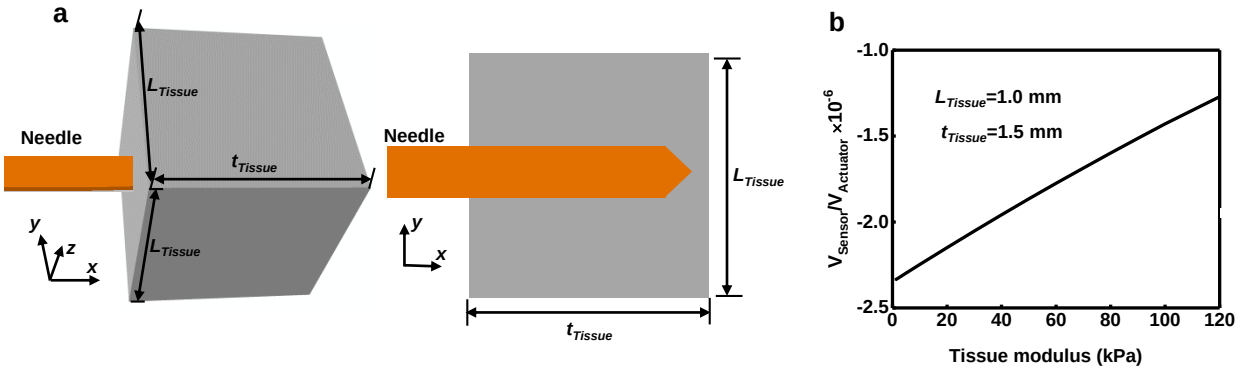

Figure S10. FEA prediction of the output voltage as a function of the tissue modulus for a small sample (size 1.0 mm × 1.0 mm × 1.5 mm)

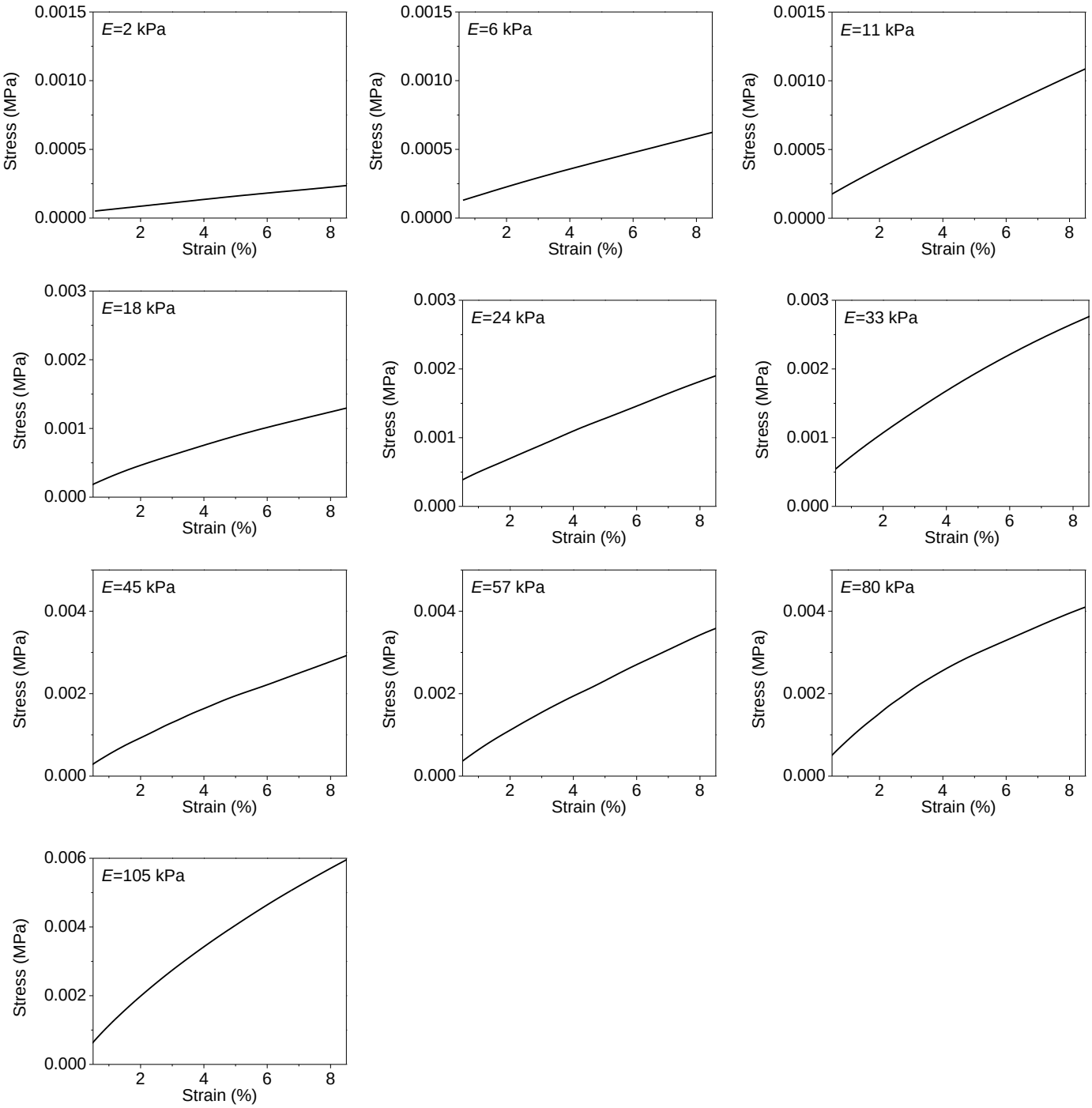

Figure S11. Tension stress-strain plots of artificial agarose gel in quasi-static strain rate regimes, with different modulus values.

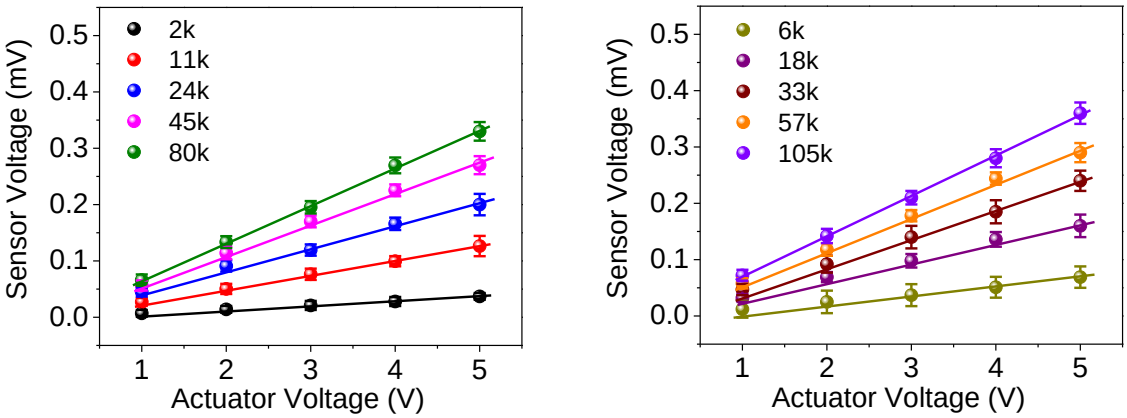

Figure S12. Experimental and theoretical analysis of the device operation. Voltage output of sensor as a function of actuator voltage, measured on ten different agarose gels with known moduli, separately evaluated by quasi-static dynamical mechanical analysis shown in Figure S10. Here, the symbols and lines correspond to experimental (E) and theoretical (T) results, respectively. Error bars correspond to calculated standard error deviation.

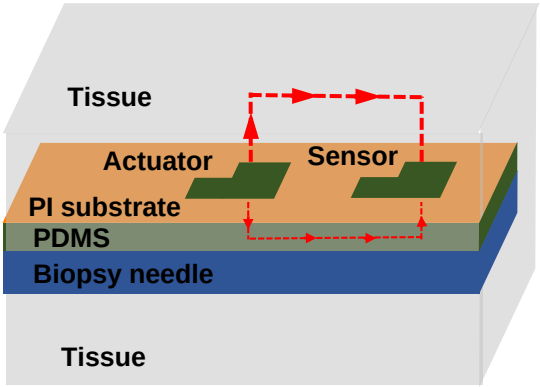

Figure S13. The mechanism of deformation for the modulus sensors integrated on a biopsy needle. The red arrows indicate that the deformation induced by the actuator is transferred to the sensor mainly via the deformation of the tissue and also the PDMS below the PI substrate

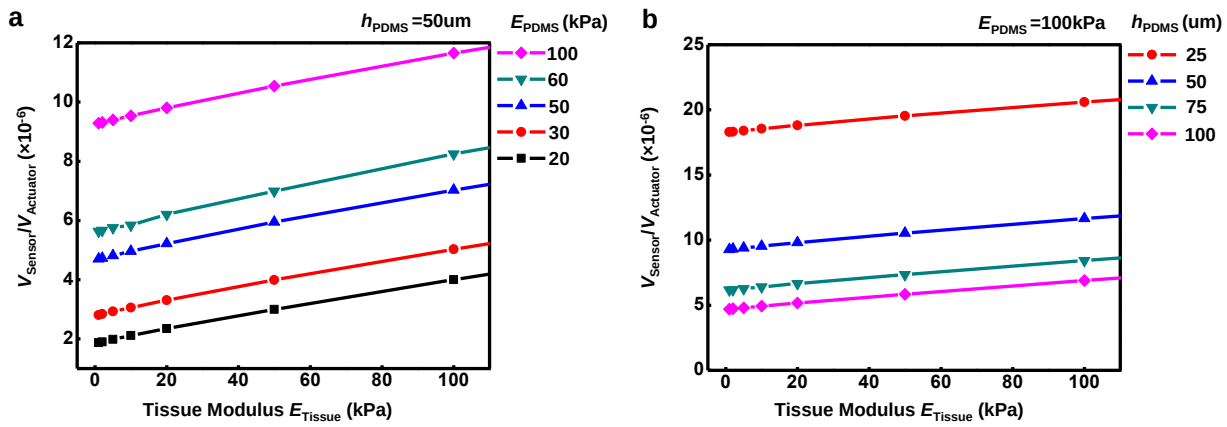

Figure S14. Theoretical analysis of biopsy needle based modulus sensor devices. a. Influence of the PDMS modulus on the sensor voltage. **b**. Influence of the PDMS thickness on the sensor voltage.

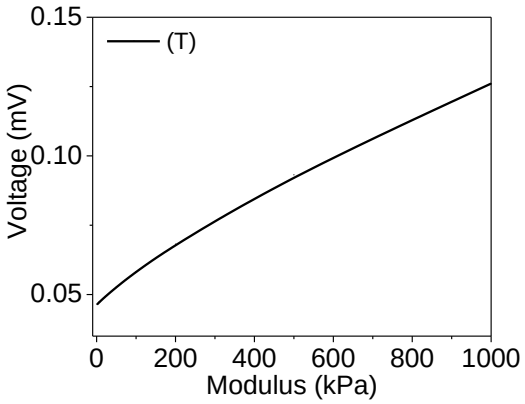

Figure S15. Theoretical analysis of V_{sensor} as a function of modulus, with actuator voltage of 5V

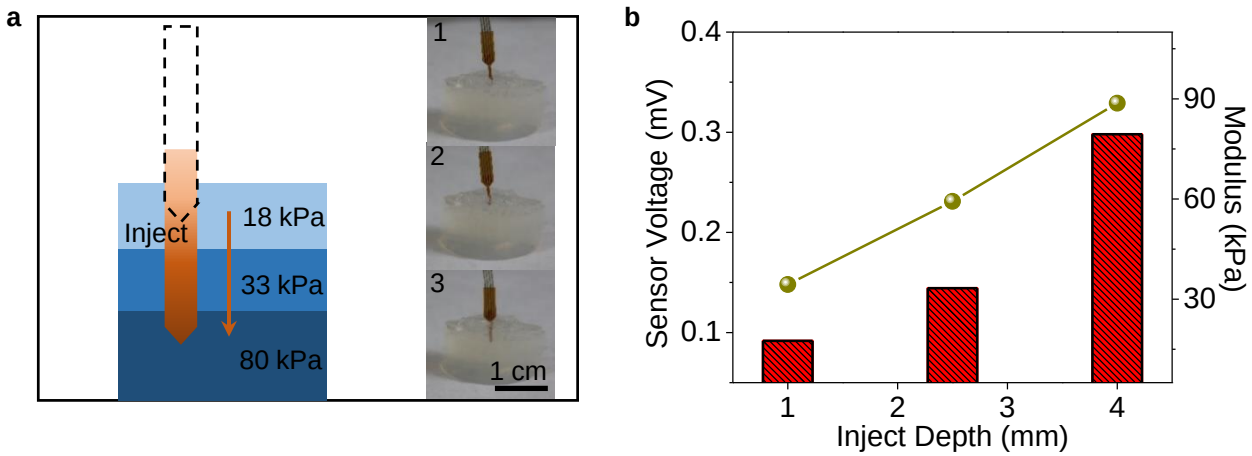

Figure S16. Experimental analysis and modulus measurements of multilayer artificial tissues. a. Modulus measurement on a multilayer sample, with three different modulus of 18, 33, and 80 kPa. **b.** Sensor voltage and modulus values at an actuation voltage of 5V, as a function of inject depth of the multilayer sample.

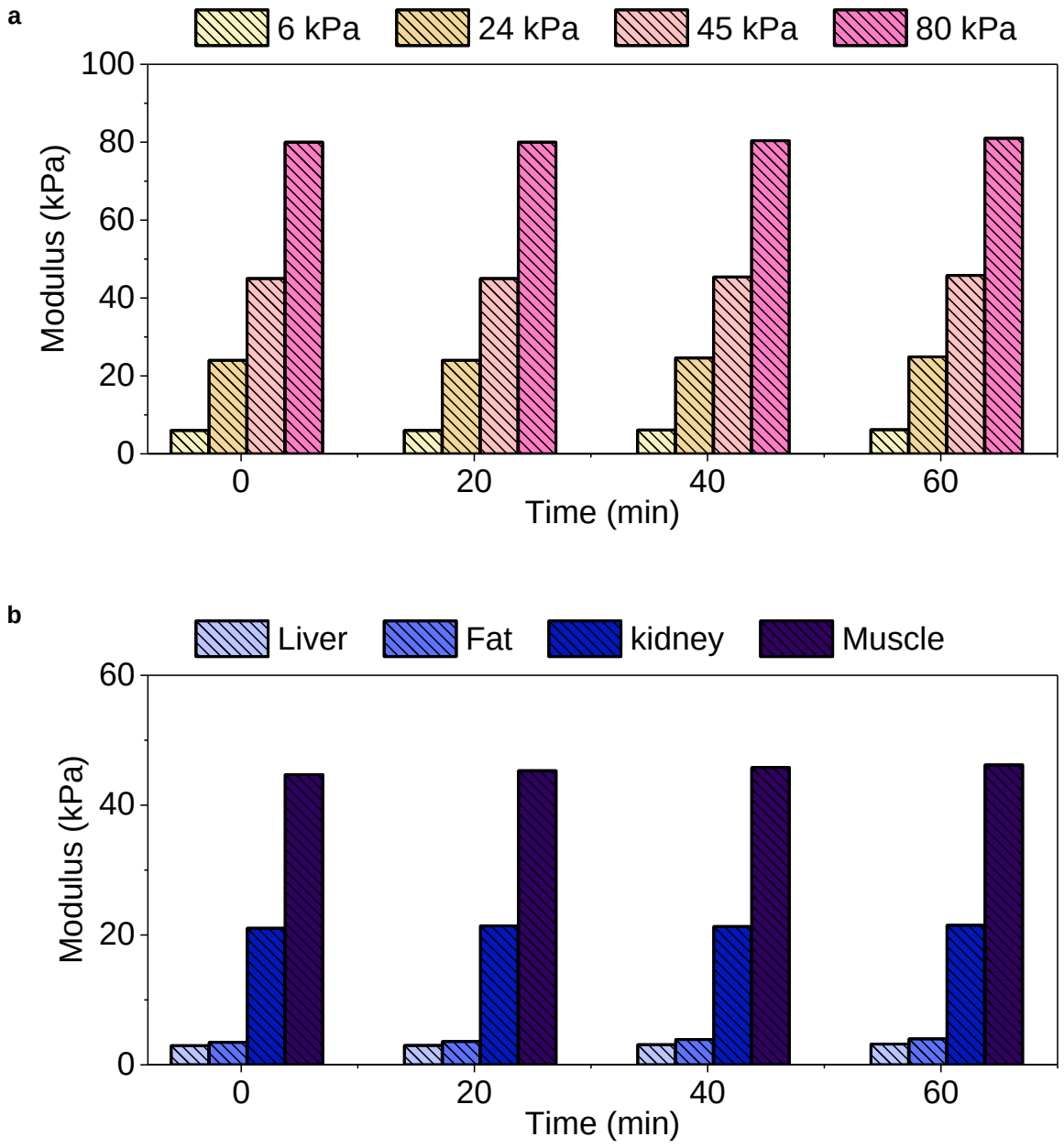

Figure S17. Modulus measurements modulus as function of time for 60 minutes. a. Measured on artificial agarose gel tissues with different modulus values. **b**. Measured on big tissues, including liver, fat, kidney, and muscle.

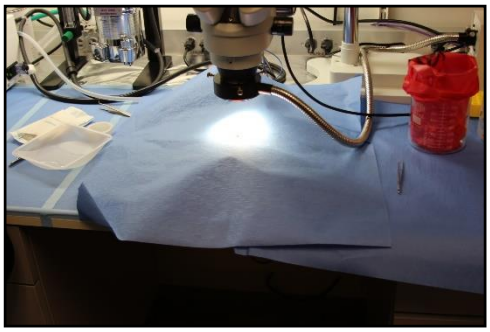

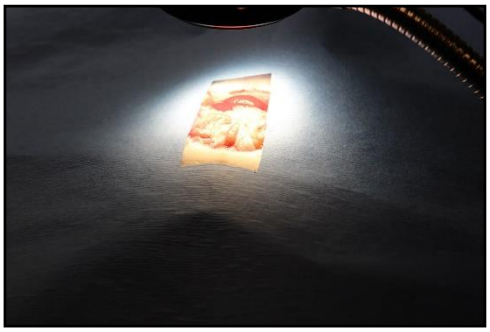

Figure S18. Illustration of surgical procedures for modulus measurement on the rat.

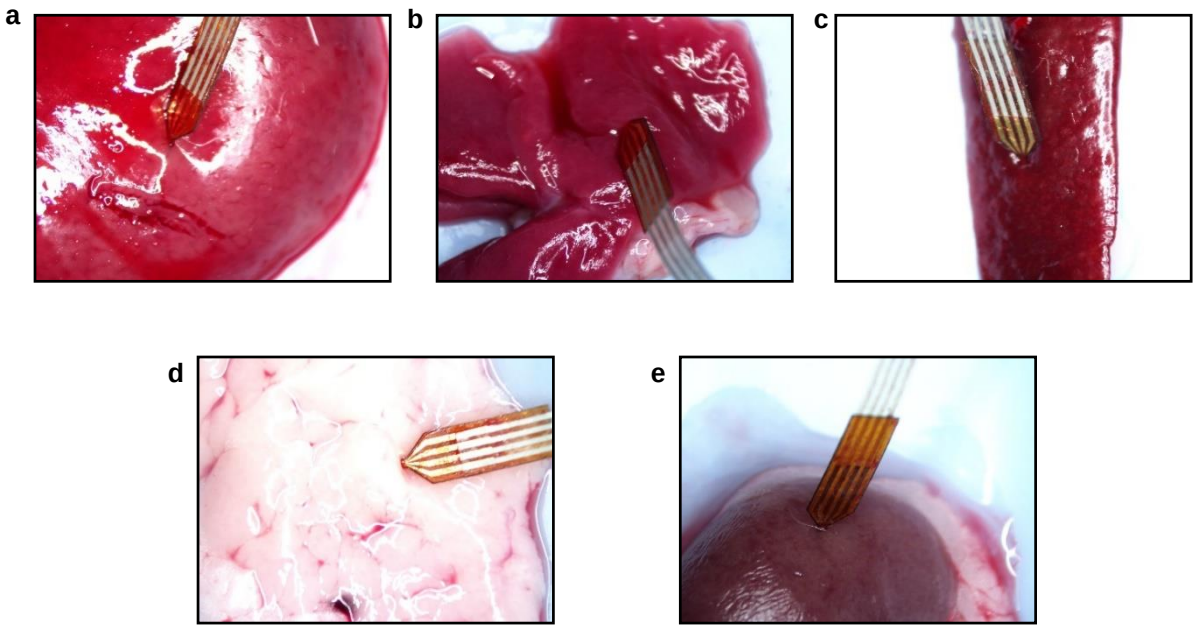

Figure S19. Ex-vivo measurement of organ tissues of the rat. Device insert and measure on liver, **a**, lung **b**, spleen **c**, fat **d**, and kidney **e**.

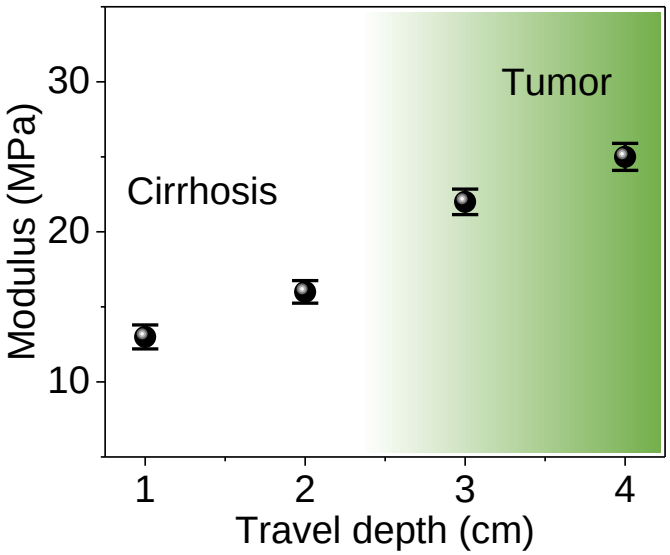

Figure S20. Real-time modulus measurement by a biopsy needle device. The device traverse from cirrhosis liver to tumor.

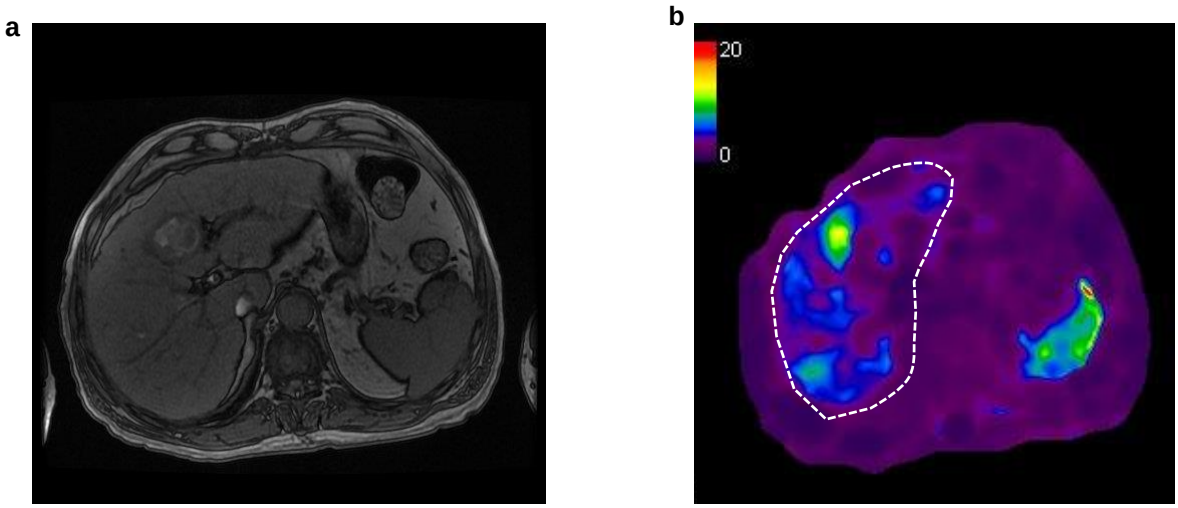

Figure S21. Images of a cirrhotic liver with hepatocellular carcinoma. a. Measured by Magnetic resonance image (MRI). **b**. Measured by Magnetic resonance electrography (MRE), shown stiffness mapping of the whole cross section of the patient.

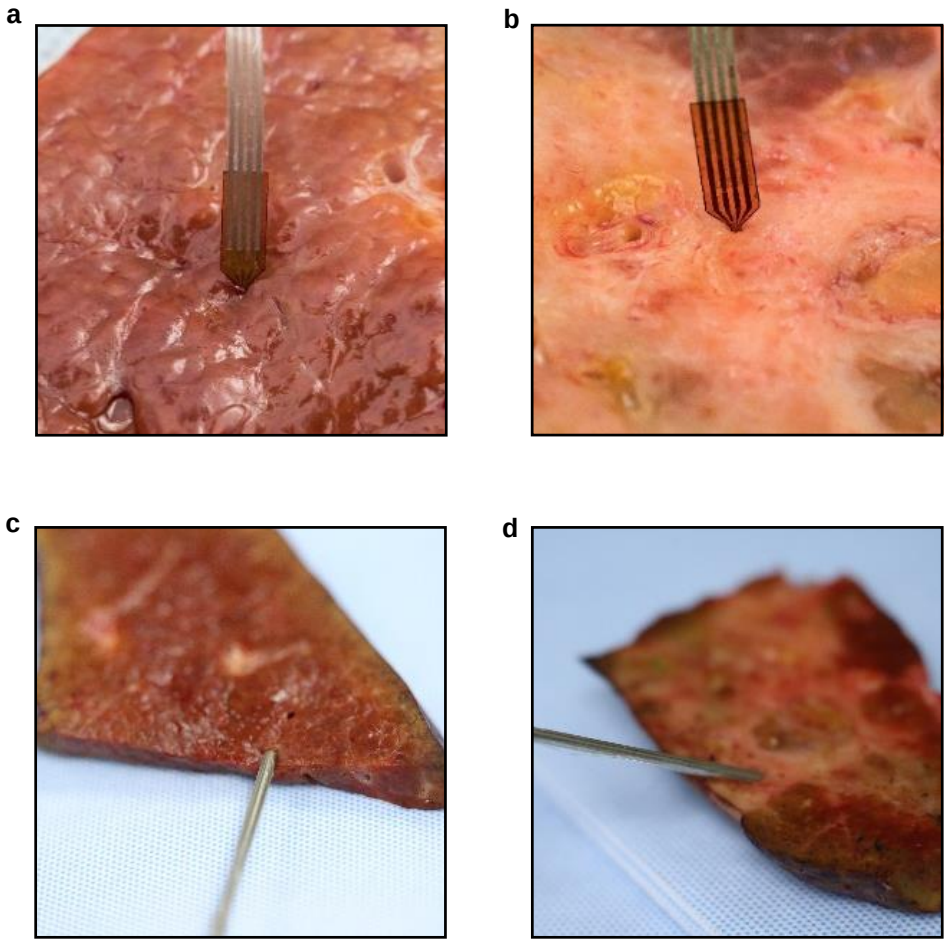

Figure S22. Image-guided modulus test. a,b, Photographs of a free standing device (device 1) injected into the non-tumor area of liver (**a**), and tumor (**b**). **c**,**d**, Photographs of a biopsy needle device (device 2) injected into the non-tumor area of liver (**c**), and tumor (**d**).